Modeling Radar Propagation in Three-Dimensional Environments

Ra'id S. Awadallah, Jonathan Z. Gehman, James R. Kuttler, and Michael H. Newkirk

APL's Tropospheric Electromagnetic Parabolic Equation Routine (TEMPER) was developed with the assumption that the terrain/ocean surface along the great circle connecting the source (radar) and the receiver (target) varies only in the range dimension. The lateral (cross-range) variations of the terrain are ignored in TEMPER. The main advantage of this assumption is that it greatly enhances the computational efficiency of the propagation model; however, it neglects the out-of-plane scattering and diffraction effects associated with lateral variations in the realistic terrain. In this article we report on the use of full three-dimensional propagation simulations to assess the impact of these out-of-plane effects on radar coverage, both in urban environments and over realistic two-dimensional digital terrain maps.

INTRODUCTION

A shipboard radar trying to interrogate a low-altitude target in a littoral environment invariably receives a signal containing the target signature buried in unwanted terrain and/or ocean clutter. This clutter results from the interaction of the radar signal with the intervening ocean surface/terrain profile as the signal propagates from the radar to the target and back. Effective detection of the target hinges on the design of appropriate clutter filters that separate the target signature from unwanted clutter. Design of the proper clutter filters requires the accurate characterization of ocean and terrain clutter, which in turn necessitates accurate prediction of the radar coverage.

Figure 1 depicts the propagation domain for radar coverage in a three-dimensional (3D) atmosphere over a two-dimensional (2D) terrain profile with hills, buildings, etc. The properties of a 3D atmosphere vary as a function of three spatial variables (x, y, z), while the height and slopes of a 2D terrain vary as a function of two spatial variables (x, y). The rigorous prediction of radar coverage over such a terrain profile entails solving the "vector wave equation," which is derived from Maxwell's electromagnetic field equations. Such a solution is challenging for two primary reasons. First, the slopes of the irregular terrain couple the three components of the vector field in an intricate fashion. Second, the inhomogeneity of the atmosphere complicates the nature of the field equations. These complications rule out analytical closed-form solutions, leaving numerical simulations as the only resort.

The numerical methods applied to the 3D propagation problem are generally categorized as integral equation methods and differential equation methods.
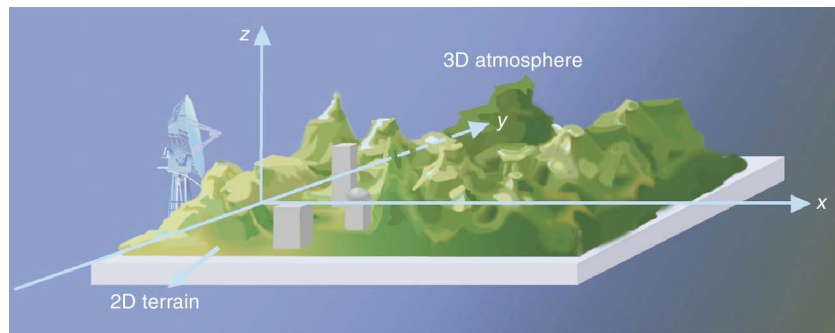
Figure 1. Typical propagation geometry for radar coverage in a 3D atmosphere over an irregular terrain profile with buildings, hills, etc.

Integral equation methods result in extremely large, full matrices that need to be inverted in order to determine the unknown fields. In addition, rigorous treatment of a general, inhomogeneous troposphere via an integral equation method is extremely difficult.[1] Consequently, this method is not the method of choice for treating long-distance radar coverage problems. Further discussion of integral equation propagation methods is beyond the scope of this article; the interested reader may consult Refs. 1 and 2 for a detailed treatment. The differential equation method, on the other hand, accounts for atmospheric inhomogeneity (ducting) in a straightforward fashion and results in sparse matrix systems that can be efficiently inverted numerically.[3] In addition, since the problem at hand involves propagation at low grazing angles, where electromagnetic energy is predominantly propagating in the forward direction, the backscattered field component can be neglected. This assumption replaces the exact vector differential wave equation with a simpler, forward-marching vector wave equation known as the vector parabolic equation (VPE).[4]

In long-distance propagation scenarios, the effects of Earth's curvature must be considered. To this end, although the final numerical calculations are conducted in a Cartesian coordinate system, the 3D propagation problem is naturally formulated in a spherical coordinate system (r, θ, ϕ), with the origin located at the Earth's center. An Earth-flattening transformation is then used to map the resulting equations onto a Cartesian coordinate system. In the spherical coordinate system, the radar transmitter is located on the z axis, and the r-θ propagation plane containing the transmitter and the receiver is located at $\phi = \phi_0 = $ constant.

Solving the full 3D vector problem for realistic radar coverage scenarios involving distances on the order of hundreds of kilometers is computationally impractical for today's desktop processors. Instead, a tractable solution can be developed by invoking two major assumptions. First, the 2D terrain surrounding the propagation plane is assumed to be azimuthally uniform and hence can be approximated by a one-dimensional (1D) terrain

slice along the great circle located within the propagation plane.[5] Second, the intervening atmosphere is assumed to be azimuthally uniform. These two assumptions decompose the original 3D propagation problem into two scalar 2D problems known as the horizontally polarized (HPOL) and the vertically polarized (VPOL) problems.[4] The HPOL problem involves a single electric field component, whereas the VPOL problem involves a single magnetic field component. Both of these components are perpendicular to the propagation plane. To further simplify the resulting 2D problems, the polar r-θ propagation plane is typically mapped onto the x-z Cartesian plane via the appropriate Earth-flattening transformation.[4] In this new coordinate system, the 1D terrain profile is a function of the range coordinate x only, while the 2D atmosphere is assumed to vary only with range x and altitude z.

The simplified 2D propagation problem described above is formulated in terms of a scalar parabolic equation (PE) governing the field components E_y (HPOL) and H_y (VPOL). This PE is amenable to efficient numerical techniques such as the split-step Fourier method (SSFM)[6,7] and the finite difference method (FDM).[4] These methods march the propagating field from the transmitter to the receiver over range increments Δx. The SSFM affords longer range steps than the FDM but requires the terrain boundary condition to be enforced on a flat boundary in the transform domain. To accommodate irregular terrain in the SSFM, a shift map is employed to flatten the terrain at the expense of modifying the governing PE.[8] The FDM, on the other hand, enforces the terrain boundary condition in the spatial domain and therefore treats irregular terrain in a more straightforward fashion.[4]

Lateral terrain uniformity is an important assumption because it facilitates the reduction of the formidable 3D vector propagation problem into a tractable 2D scalar problem. This assumption is reasonable in scenarios involving smooth terrain profiles, where out-of-plane scattering and diffraction effects caused by lateral terrain slopes are negligible. In scenarios involving steep terrain features, such as propagation in urban environments, substantial out-of-plane scattering will take place, rendering the 2D assumption inadequate. In this article, the lateral terrain effects on the field propagating in a 3D environment are investigated via direct propagation simulations. Two types of 3D domains are examined: an urban environment and a digital terrain map. The full 3D VPE results are compared with results obtained via a pseudo-3D version of the 2D propagation model TEMPER (Tropospheric Electromagnetic Parabolic

Equation Routine), referred to herein as P3DTEMPER, which is implemented by running 2D TEMPER on multiple azimuths that span the 3D domain of interest and combining the azimuths to approximate propagation in a 3D environment.[9]

THE VECTOR PARABOLIC EQUATION PROPAGATION MODEL

Recall that the VPE is based on the assumption that the radar wave energy propagates predominantly in the forward direction. This assumption is good for low-grazing-angle propagation over a smooth terrain or ocean surface where the small backscattered field component can be neglected. The propagation domain used in this article is rectilinear, where x, y, and z represent the range, cross-range, and altitude coordinates, respectively (Fig. 2). In this propagation domain, the VPE governing the vector field propagating forward away from the source (radar) is given, in free space, by

$$\frac{\partial \mathbf{E}}{\partial x} = i \sqrt{k^2 + \frac{\partial^2}{\partial y^2} + \frac{\partial^2}{\partial z^2}}\, \mathbf{E}. \qquad (1)$$

The standard VPE (SVPE), also known as the narrow-angle VPE, is derived from Eq. 1 by using the binomial expansion to replace the radical and keeping the first two terms in the expansion. The SVPE is given by

$$\frac{\partial \mathbf{E}}{\partial x} = \frac{i}{2k}\left(\frac{\partial^2}{\partial y^2} + \frac{\partial^2}{\partial z^2} \right)\mathbf{E} + ik\mathbf{E}. \qquad (2)$$

In Eqs. 1 and 2, the electric field $\mathbf{E}$ has three components, E_x, E_y, and E_z; $k = 2\pi/\lambda$ (λ is the radar operating wavelength); and $i = \sqrt{-1}$. Equation 1 propagates the field from the source plane (Plane A) to the subsequent planes (B, C, etc.).

The propagating field is subject to the terrain boundary condition, which represents the relationship that must hold between the different field components at the different points of the irregular terrain. For highly conducting terrain, a simple approximate form of the terrain boundary condition known as the impedance boundary is given by

$$\hat{\mathbf{n}} \times \mathbf{E} = Z\hat{\mathbf{n}} \times (\hat{\mathbf{n}} \times \nabla \times \mathbf{E}). \qquad (3)$$

In Eq. 3, the terrain impedance is given by $Z = 1/(ik\sqrt{\epsilon_r})$, where ϵ_r is the dielectric permittivity of the terrain, and $\hat{\mathbf{n}}$ is the outward unit normal vector to the terrain surface. When numerical propagation simulations are performed, infinite propagation domains cannot be realized and the size of the propagation domain must be truncated. This is accomplished numerically by enforcing an absorbing boundary condition on the upper and two vertical sides of the propagation domain exhibited in Fig. 2. This absorbing boundary condition truncates the propagating field smoothly to zero outside the propagation domain and prevents artificial reflections from the domain numerical boundaries. Currently, the absorbing boundary condition is most popularly implemented by lining the upper and vertical sides of the propagation domain with perfectly matched layers (PMLs).[10] In this article, we adopt the simple PML formalism proposed by Rappaport.[11] A typical propagation plane exhibiting a lateral slice of the terrain and the PMLs described above is shown in Fig. 3.

In the absence of the terrain, the individual components of the electric field can be propagated independently from a typical propagation plane to the subsequent
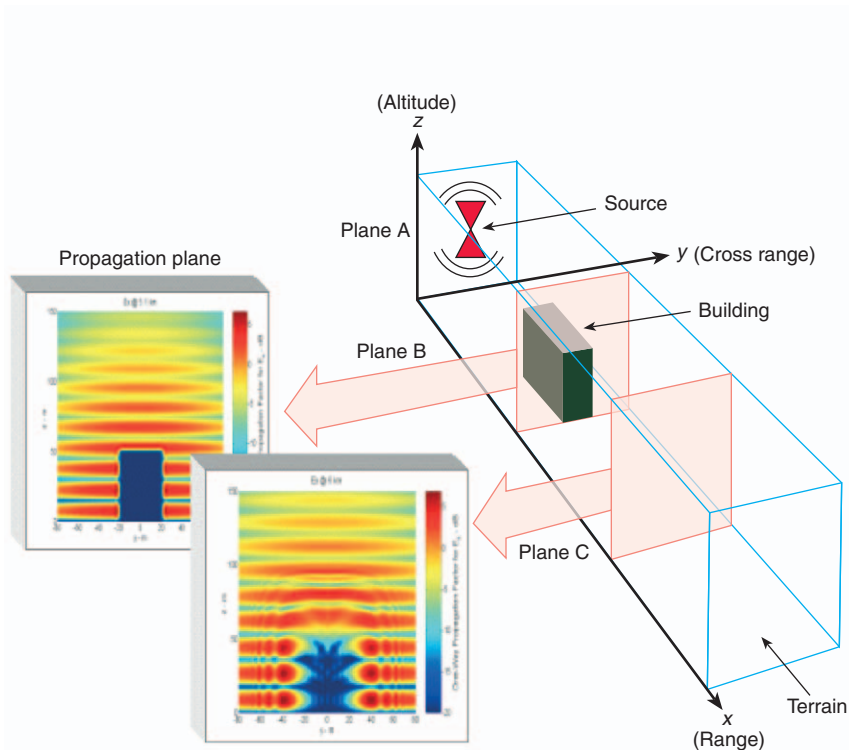

Figure 2. Propagation domain used for the vector parabolic equation (VPE) numerical simulations. The VPE model marches the radar field from the source plane (Plane A containing the radar antenna) to subsequent range planes B, C, etc.
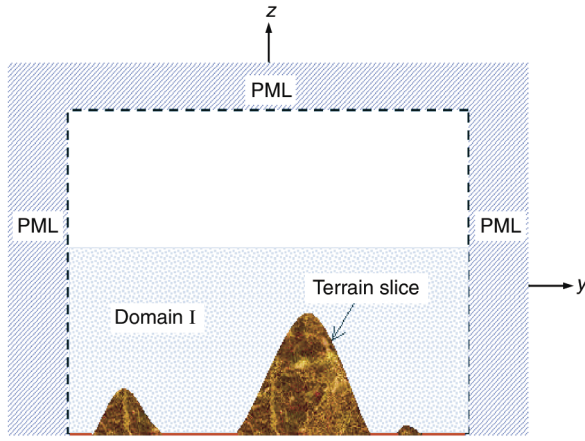
Figure 3. A typical VPE propagation plane displaying the terrain slice contained in that plane and the perfectly matched layers (PMLs) used to eliminate nonphysical reflection artifacts from the plane boundaries. In this propagation plane, Domain I is the region surrounding the terrain slice.

plane in range. This is accomplished by marching the Cartesian components of the VPE (Eq. 1) in range via either the SSFM or the FDM. Because of its suitability for treating boundary conditions on 2D irregular terrain configurations, the FDM is our method of choice in this article.

Marching Eq. 1 in range using the FDM starts by the formal solution of Eq. 1 given by

$$\psi(x + \Delta x, y, z) = \exp\left[i\Delta x \sqrt{k^2 + \frac{\partial^2}{\partial z^2} + \frac{\partial^2}{\partial y^2}}\right] \quad (4)$$
$$\times \psi(x, y, z),$$

where $\psi = E_x, E_y, E_z$, and Δx is the range increment. Clearly the formal solution (Eq. 4) relates the field ψ at the advanced propagation plane located at range $x + \Delta x$ to the field computed at the current propagation plane x. The FDM cannot be applied to Eq. 4 in its current form since the z and y derivatives in the equation are coupled and appear under the radical. The derivative operators in Eq. 4 are decoupled via the approximation

$$\sqrt{k^2 + \frac{\partial^2}{\partial z^2} + \frac{\partial^2}{\partial y^2}} \approx \sqrt{k^2 + \frac{\partial^2}{\partial z^2}} + \sqrt{k^2 + \frac{\partial^2}{\partial y^2}} - k. \quad (5)$$

Substituting Eq. 5 into Eq. 4 we obtain

$$\psi(x + \Delta x, y, z) = \exp\left[i\Delta x \sqrt{k^2 + \frac{\partial^2}{\partial z^2}}\right]$$
$$\times \exp\left[i\Delta x \sqrt{k^2 + \frac{\partial^2}{\partial y^2}}\right]\psi(x, y, z). \quad (6)$$

In Eq. 6, a constant phase factor $\exp(-ik\Delta x)$ has been suppressed. Furthermore, to eliminate the radicals in

the equation, we approximate the individual exponentials by a rational function via a suitable Padé approximation.[12] This Padé approximant replaces the first exponential by rational functions of the derivative operator $\partial^2/\partial z^2$, with the numerator of this function being linear in $\partial^2/\partial z^2$ and the denominator being quadratic in $\partial^2/\partial z^2$. The same method is applied to the second exponential. Applying the suitable Padé approximant to Eq. 6 reduces it to a form that can be discretized via finite differences, yielding a product of four tridiagonal systems of equations that can be inverted in sequence to obtain the field at the advanced plane located at range $x + \Delta x$.[13]

The presence of the 2D terrain complicates the propagation problem by coupling the different field components according to the boundary condition (Eq. 2). The simple marching technique described above is not applicable in the presence of the terrain. The effect of the terrain on the propagating field can be accounted for by employing the following hybrid model, which is based on the field equivalence principle.[14] This hybrid model propagates the field from the current propagation plane to the subsequent plane in two steps.[15] First, the terrain is removed and the field is propagated from the previous plane to the current plane via the marching technique described above. Second, the terrain slice located in the current propagation plane is restored and the coupled field problem governed by the SVPE (Eq. 2) and the boundary condition (Eq. 3) is re-solved in Domain I, which contains the terrain slice (Fig. 3). The field values within Domain I obtained by the first step are replaced by those obtained by the second step; then the procedure is repeated to propagate the field to the subsequent planes. The solution in the second step is carried out as follows. The governing SVPE (Eq. 2) and the boundary condition (Eq. 3) are discretized using finite differences, resulting in a sparse system of equations of the form

$$\mathbf{Ax} = \mathbf{b}. \quad (7)$$

Equation 7 is solved for the unknown vector field $\mathbf{x}$ in Domain I via an iterative procedure such as the preconditioned biconjugate gradient method.[16] Since the matrix $\mathbf{A}$ is sparse, only the nonzero entries of $\mathbf{A}$ need to be stored. This can be accomplished by using the row-index storage format.[16] The SVPE (Eq. 2) is used instead of the exact VPE (Eq. 1) in the second solution because the second solution step is carried out in the current propagation plane, where the field information needed to represent the range derivative ($\partial/\partial x$) by finite differences is not available. To accurately estimate $\partial/\partial x$, one needs the field values in the previous, current, and next propagation planes. The field values both at the current and next planes are not known, and the direct implementation of the range derivative is not recommended.[4] Instead, one needs to replace $\partial/\partial x$ in terms of

$\partial/\partial y$ and $\partial/\partial z$ in order to express the boundary condition in terms of transverse derivatives in the current propagation plane. This replacement is only possible by using the SVPE. The height of Domain I is chosen such that the terrain points have minimal effect on the field points located above Domain I of the current propagation plane (Fig. 3).

PSEUDO-3D TEMPER MODEL

The 2D TEMPER model solves the scalar version of the VPE (Eq. 1), without the cross-range derivative operator $\partial^2/\partial y^2$, using the SSFM.[17] Propagation over 2D terrain can be simulated by running TEMPER over multiple 1D azimuths (red lines in Fig. 4) with the terrain assumed to be 1D (corrugated) along each azimuth. The 2D (x, z) propagation data from these azimuths are then combined to approximate propagation in a 3D environment. It is evident that this approach does not capture out-of-plane scattering and diffraction effects; however, TEMPER does model forward scatter and diffraction caused by the in-plane terrain variations.

Two terrain models are currently implemented in TEMPER. The first is the linear-shift map model proposed by Donohue and Kuttler.[8] This model, which is accurate for terrain slopes less than about 15°, replaces the irregular terrain by a set of piecewise linear segments. Terrain profiles with steeper slopes are modeled using the knife-edge (KE) approximation. This approximation represents the terrain by a series of perfectly conducting KEs, where the propagating field is replaced by the null field at and below the terrain point coinciding with the current range point, and the resulting field is then propagated to the next range point.

Using a combination of these two terrain models (linear-shift map for terrain slopes < 15° and KE for larger terrain slopes), TEMPER can account for in-plane terrain effects. TEMPER has also been shown to very accurately model tropospheric refraction effects. Because of its accuracy and numerical efficiency, TEMPER is currently used by the Navy community to model site-specific 3D scenarios. Not being able to account for out-of-plane scattering and depolarization effects is a limitation that must be tolerated, as rigorous 3D modeling of these scenarios would be computationally prohibitive. Because the 2D assumption will persist for years to come, even with foreseeable advances in processor speed, it is important to quantify and understand the errors it entails.

SOURCE MODELING

Meaningful comparisons between the P3DTEMPER and the full VPE model are achievable only when the two codes propagate the same source field. For the numerical simulations reported in this article, the VPE model uses a 2D rectangular antenna aperture with a
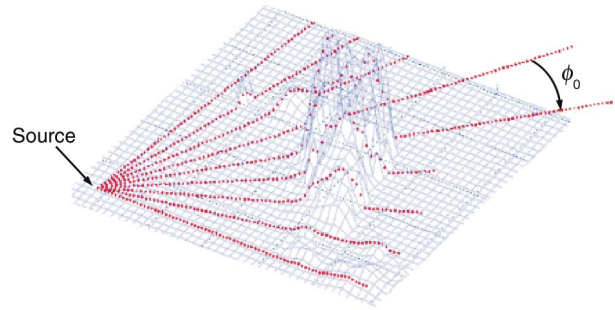

Figure 4. The propagation geometry for P3DTEMPER. The red lines indicate the different propagation azimuths along which the P3DTEMPER model runs to approximate propagation in a 3D environment.

Gaussian-shaped aperture (source) field. This 2D source is illustrated in Fig. 5a. Starting with the 2D source distribution, one needs to calculate the proper 1D aperture source distributions that give rise to the fields propagating along each azimuth in the P3DTEMPER scheme. This task can be accomplished as follows. A 2D Fourier transform is used to calculate the 3D far-field pattern associated with the 2D aperture distribution. Since the source distribution is Gaussian, the far-field pattern is also Gaussian. This far-field pattern as a function of the polar angle θ (measured from the z axis) and the azimuth angle ϕ (measured from the x axis) is shown in
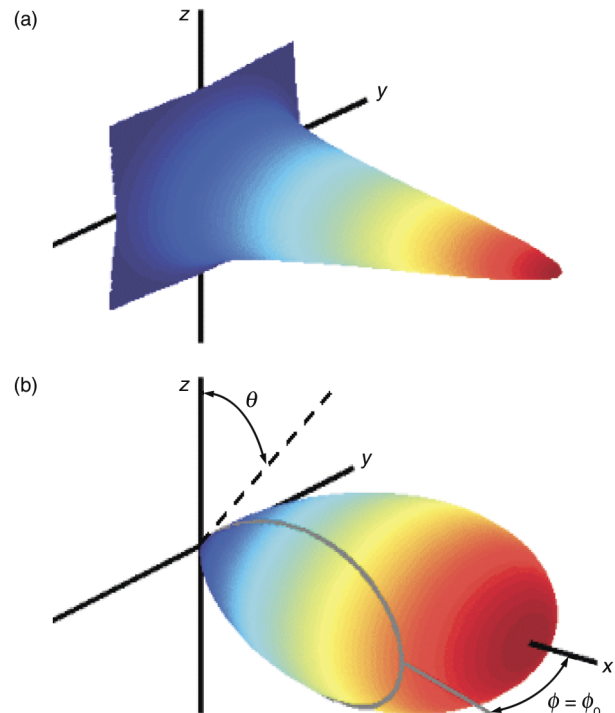

Figure 5. (a) 2D radar antenna with Gaussian aperture source distribution. The Gaussian source distribution was chosen for ease of mathematical analysis. The VPE model presented herein works equally well for any smooth source distribution. (b) The 3D far-field pattern of the 2D Gaussian source distribution. The far-field pattern of an antenna is given by the Fourier transform of the aperture source distribution.
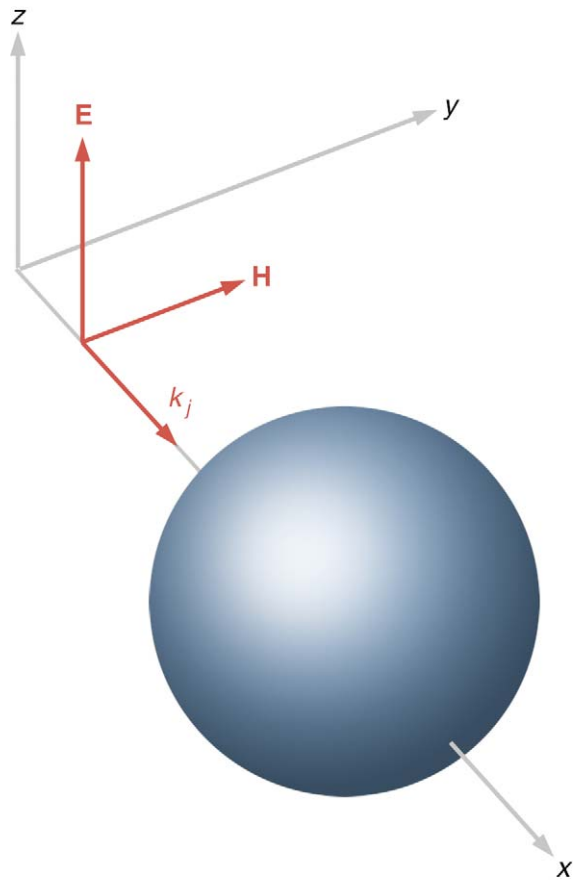
Figure 6. Geometry for VPOL plane-wave scattering from a perfectly conducting sphere. The incident plane wave (k_j) is propagating along the x axis. The radius of the sphere is 5 λ, where λ is the radar operating wavelength. (**E** = electric field, **H** = magnetic field.)

Fig. 5b. To perform a P3DTEMPER calculation along a specific azimuth $\phi = \phi_0$, the far-field pattern slice at ϕ_0 is inverse Fourier transformed to determine the 1D aperture distribution responsible for that slice. The complete far-field pattern is then synthesized by repeating this process for all azimuths to be considered in a given propagation scenario.

In the numerical examples discussed below, a HPOL source field is one that has a single y-directed electric field component, while a VPOL source field has a single z-directed magnetic field component.

NUMERICAL SIMULATIONS AND DISCUSSION

In the examples that follow, the VPE model's solution is taken as "ground truth" reference for P3DTEMPER. In this way, full 3D terrain effects are compared to their 2D approximants. To perform these comparisons with confidence, we first assess the VPE model's two-step, wide-/narrow-angle handling of propagation over irregular terrain by benchmarking the VPE model against

the exact Mie-series solution of scattering from a perfectly conducting sphere. The scattering geometry—a VPOL plane electromagnetic wave incident on a perfectly conducting sphere of radius $a = 5$ λ—is shown in Fig. 6. The total z-directed field was calculated, using both the exact Mie-series expansion and the VPE model, at a distance of 30 λ behind the sphere. These results are plotted in Figs. 7a ($z = 0.1$ λ) and 7b ($y = 0.1$ λ). Despite using a narrow-angle propagator for terrain effects, the VPE model agrees well out to distances corresponding to nearly 35° from the horizontal (x axis).

The first simulation example involves propagation over the simple notional urban terrain illustrated in Fig. 8. This "terrain" consists of eight buildings on a flat plane, arranged in two rows centered on $y = +50$ m and $y = -50$ m. Each building is 50 m tall, 40 m wide, and 200 m deep. The source field is a HPOL Gaussian beam centered at (0, 0, 30 m) and has a $1/e$ beamwidth of 6 m. The material composing the buildings and the flat terrain beneath is assumed to be highly conducting, with a complex relative permittivity $\epsilon_r = 80 + i79.1$. In this and
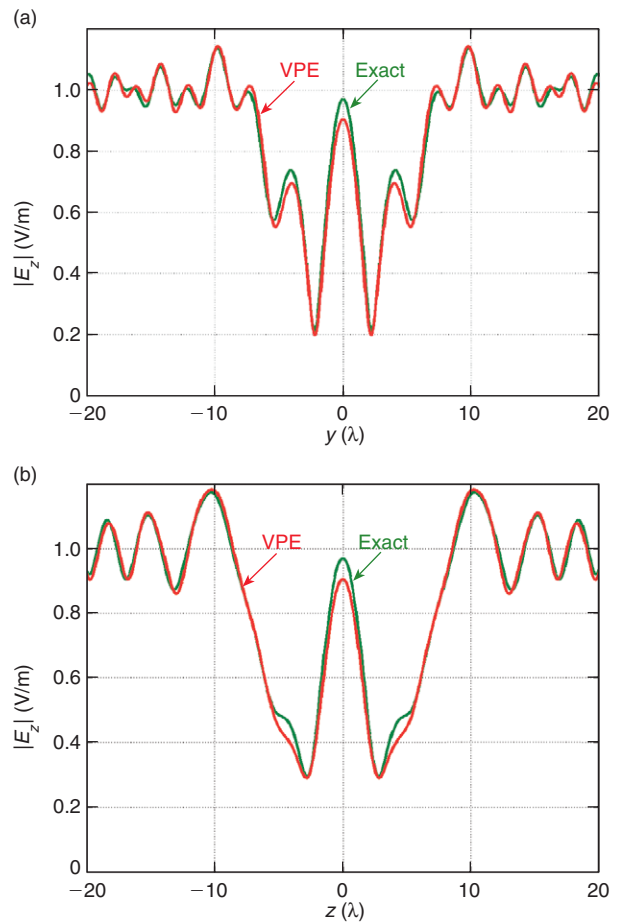

Figure 7. Magnitude of the total E_z (a) as a function of y at $x = 30$ λ and $z = 0.1$ λ behind the sphere of Fig. 6 and (b) as a function of z at $x = 30$ λ and $y = 0.1$ λ behind the sphere of Fig. 6. The exact field was calculated via the Mie series.
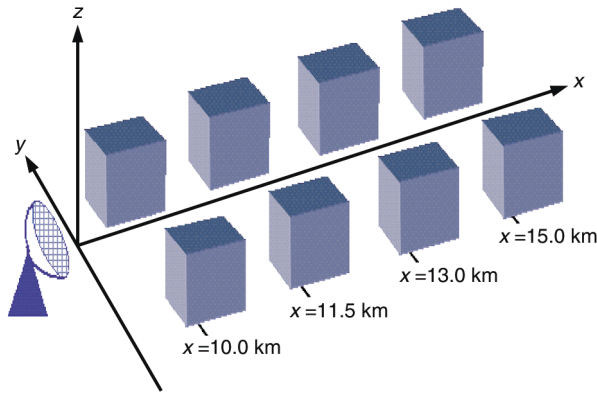
Figure 8. A simple urban propagation environment composed of a flat terrain with four pairs of buildings. Each building is 50 m tall, 40 m wide, and 200 m deep.

Figure 9. The one-way propagation factor (OWPF) obtained by (a) the VPE model and (b) the P3DTEMPER model plotted in the three orthogonal planes: the x plane is located at $x = 18$ km, the y plane at $y = 80$ m, and the z plane at $z = 10$ m for the urban terrain example depicted in Fig. 8.

all other numerical examples cited in this section, the operating frequency is taken to be 1 GHz.

For visual clarity and to display the 3D propagating field in a manner suitable for comparisons, the plotted quantity is the one-way propagation factor (OWPF):

$$OWPF = 20\log_{10}(x|E_p|), \; p = \begin{cases} y, HPOL \\ z, VPOL \end{cases}. \quad (8)$$

Plots show model output, in terms of OWPF, at three orthogonal slices through the solution volume: x planes ($x =$ constant), y planes ($y =$ constant), and z planes ($z =$ constant). Figures 9a and 9b display three orthogonal slices calculated by the VPE and P3DTEMPER model, respectively, in the notional urban environment. These slices are located at $x = 18$ km, $y = 80$ m, and $z = 10$ m. In Fig. 9a, the deep blue regions on the z plane indicate the location of the buildings. The white regions on the z plane in Fig. 9b indicate the same locations. The strong out-of-plane scattering and diffraction by the vertical side edges of the building are clearly displayed in the VPE results of Fig. 9a. The out-of-plane diffracted field fills in the shadow regions behind the buildings, and out-of-plane scattering interferes with the direct field propagating between the two rows of buildings. These effects are absent in Fig. 9b because of the 2D nature of the P3DTEMPER.

These differences are even more evident in line-plot comparisons. Figure 10 contains cross-range line cuts across the x-plane slices shown in Figs. 9a and 9b. These line cuts are taken at $x = 18$ km and $z = 10$ m. Out-of-plane diffraction effects are manifested most dramatically in the shadow regions behind the last two buildings (-100 m $< y < -40$ m and 40 m $< y < 100$ m in Fig. 10a). Figure 10b displays altitude cuts through the slices shown in Figs. 9a and 9b (at $x = 18$ km and $y = 80$ m). Again, the difference between the VPE result and the P3DTEMPER result is most pronounced in the shadow region behind the last building ($z < 50$ m in Fig. 10b).
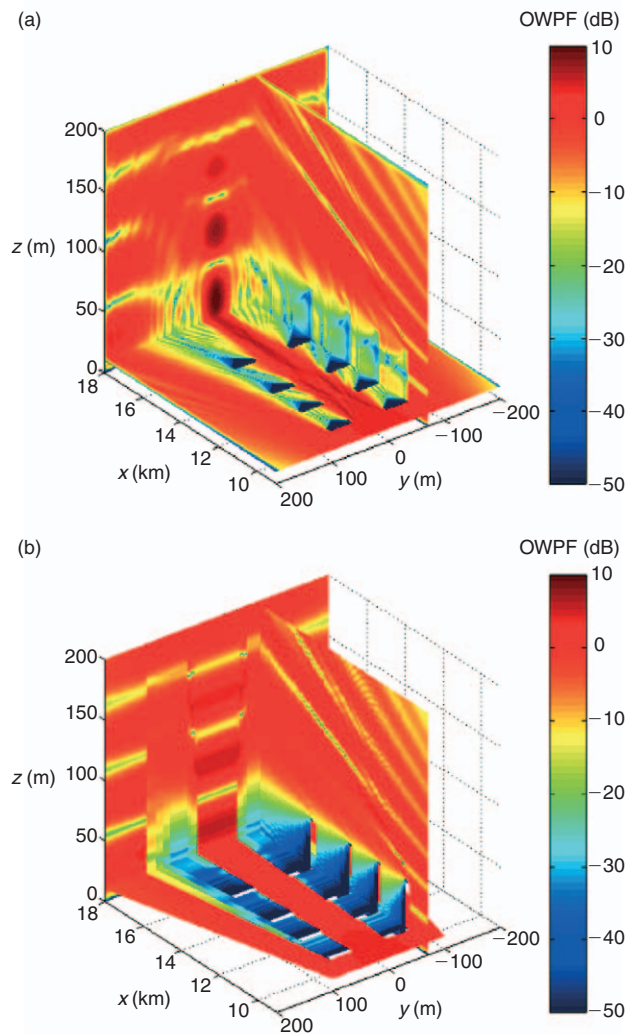
A more thorough, quantitative comparison is displayed in Fig. 11. This plot contains the point-for-point OWPF difference between VPE and P3DTEMPER at $x = 18$ km (i.e., difference between the x planes shown in Figs. 9a and 9b). Through careful manipulation of the P3DTEMPER calculation grid, no interpolations were required to compute Fig. 11; all errors are purely a result of 2D versus 3D propagation. Whether these errors occur at low or high power levels can be discerned from Fig. 12, which shows a bivariate histogram of the OWPF differences displayed in Fig. 11 as a function of the OWPF predicted by the VPE model. The histogram reveals discrepancies on the order of 6 dB occurring at high VPE power levels, rough agreement (within ±5 dB) at intermediate powers, and significant differences (3D results 5 to 15 dB higher than 2D results) at lower VPE power levels (OWPFs of −15 to −5 dB). The differences occurring at high power levels can be attributed to
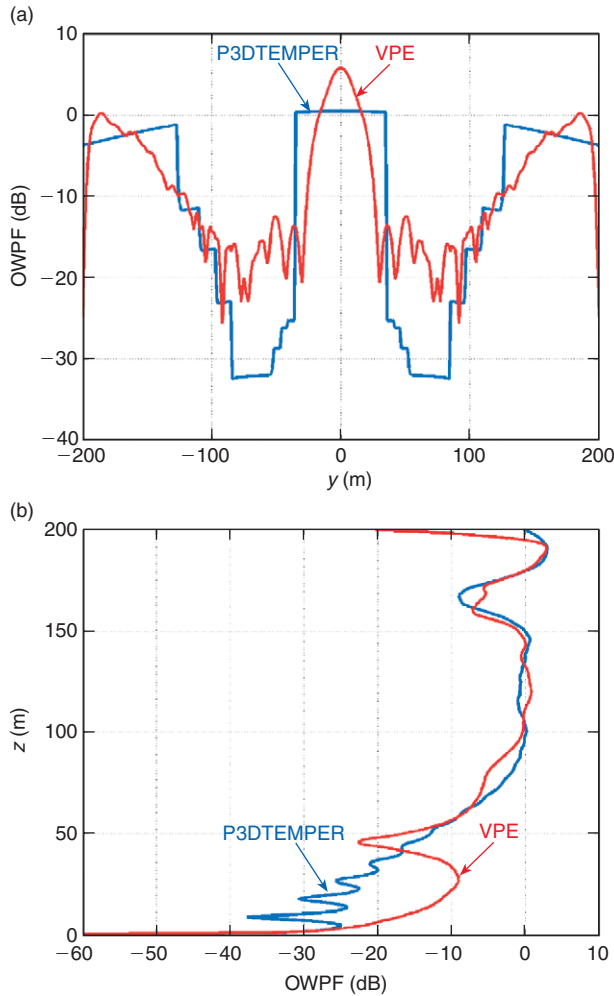
(a)

(b)

Figure 10. The OWPF (a) as a function of cross-range y at range $x = 18$ km and altitude $z = 10$ and (b) as a function of altitude z at range $x = 18$ km and cross-range $y = 80$ for the urban terrain example depicted in Fig. 8.
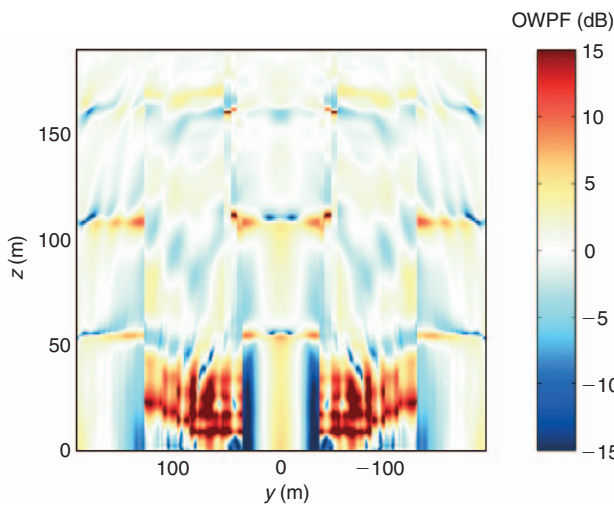

Figure 11. The decibel difference between the OWPF calculated by VPE and that calculated by P3DTEMPER at the $x = 18$-km plane. Results are for the urban terrain configuration shown in Fig. 8.
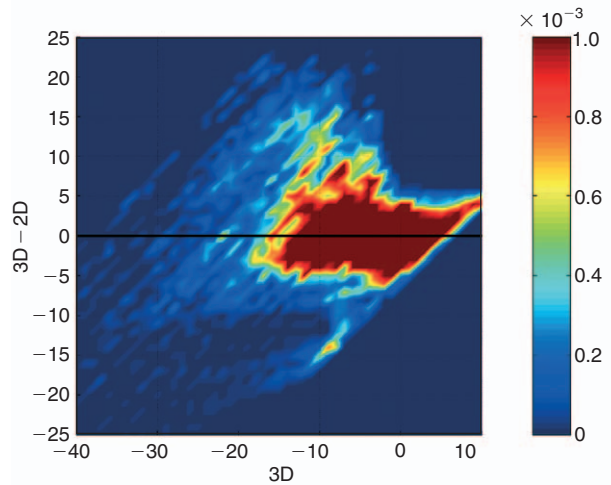

Figure 12. A bivariate histogram of the OWPF decibel difference displayed in Fig. 11 (vertical axis) as a function of the VPE OWPF in decibels (horizontal axis). Results are for the urban terrain configuration shown in Fig. 8.

constructive interference of the out-of-plane fields scattered by the vertical sides of the buildings, while the differences at the low power levels are attributable to lateral diffraction into the shadow regions by the vertical edges of the buildings.

Naturally, there are pronounced differences between the VPE and P3DTEMPER for the notional urban scenario because of the sheer vertical features in the terrain surface. The next example investigates whether these differences persist for more natural terrain, where large-scale steep vertical features are not present. Figure 13 shows the small matrix of digital terrain used for this example: a hill at the southern tip of Ni'ihau Island, Hawaii, that extends roughly 1 km in range (x) and 800 m in cross range (y), and peaks at 170 m above sea level. Digital terrain was obtained at a horizontal resolution of 10 m and then linearly resampled at 1-m intervals for use in VPE. The VPE model's propagation domain was 22 km in range, 800 m in cross range, and 250 m in altitude. The digital terrain swath was placed between $x = 18$ km and $x = 19$ km in the propagation domain and surrounded by a flat ocean surface. This surface is illuminated by a VPOL source field with an operating frequency of 1 GHz.

Figures 14a and 14b exhibit three orthogonal OWPF slices, analogous to those of Figs. 9a and 9b, computed by VPE and P3DTEMPER, respectively. In Figs. 14a and 14b, the slices are located at $x = 22$ km, $y = -150$ m, and $z = 40$ m. In contrast to the urban terrain results of Figs. 9a and 9b, the OWPF differences are not as pronounced in this example. This is simply a result of the lack of steep terrain features in the terrain under consideration. Out-of-plane scattering is minimal, and diffraction effects are mainly caused by smooth surface diffraction, which is weaker than the sharp-edge diffraction present in the urban terrain example.
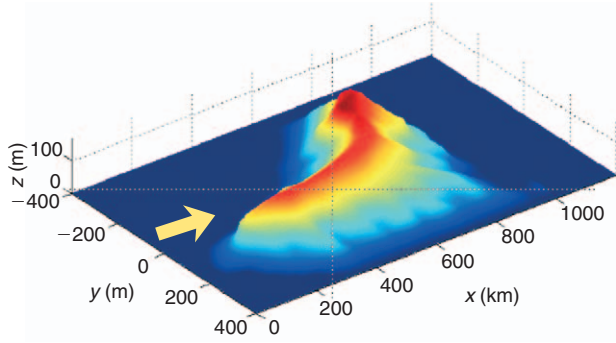
Figure 13. A slice of the southern part of Ni'ihau Island, Hawaii. The arrow indicates the direction of the source radar beam.
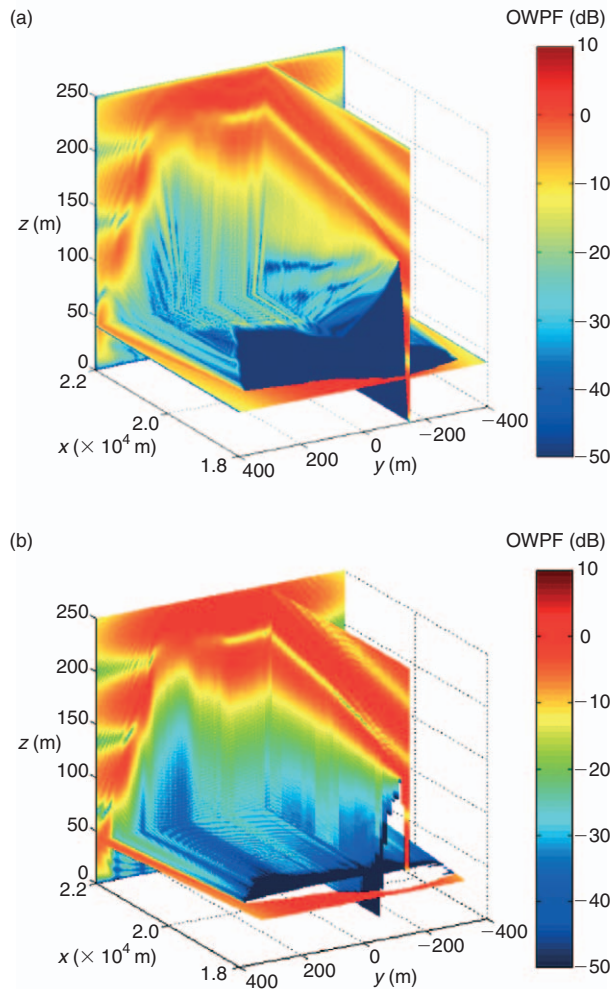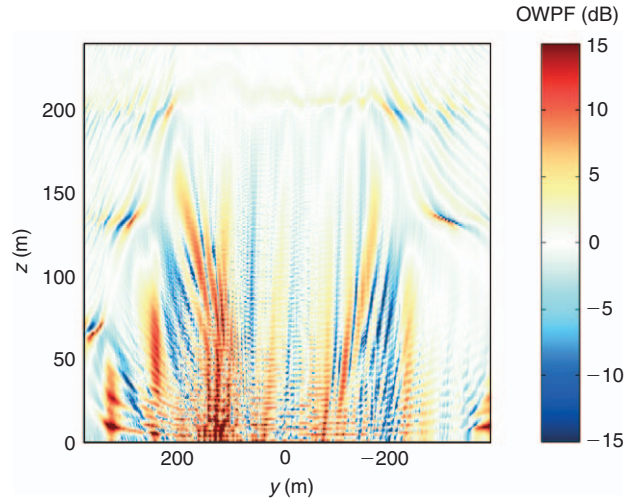

Figure 15. The decibel difference between OWPF calculated by VPE and that calculated by P3DTEMPER at the $x = 22$-km plane. Results are for the Ni'ihau Island scenario shown in Fig. 13. The polarization is VPOL.

Figure14. The OWPF obtained by (a) the VPE model and (b) the P3DTEMPER model plotted in the three orthogonal planes: the x plane is located at $x = 22$ km, the y plane at $y = -150$ m, and the z plane at $z = 40$ m for the digital terrain map of Fig. 13.

15 dB) do occur at lower power levels (OWPFs of -15 to -30 dB). These differences, which are evident as vertical lines in the difference plot of Fig. 15, occur mainly in the deep shadow region behind the hill (blue regions of the x plane shown in Fig. 14).

The accuracy of P3DTEMPER in the digital terrain example was remarkably good; however, out-of-plane diffracted/scattered fields in wider terrain swaths might accumulate to more appreciable levels at certain locations as a result of constructive interference. Hence, larger and more intricate digital terrain maps must be considered before the above conclusion can be generalized. Having stated this important caveat, it is interesting to note that the small lateral field variations exhibited in the digital terrain example agree with the order-of-magnitude estimates reported by Fock.[5]
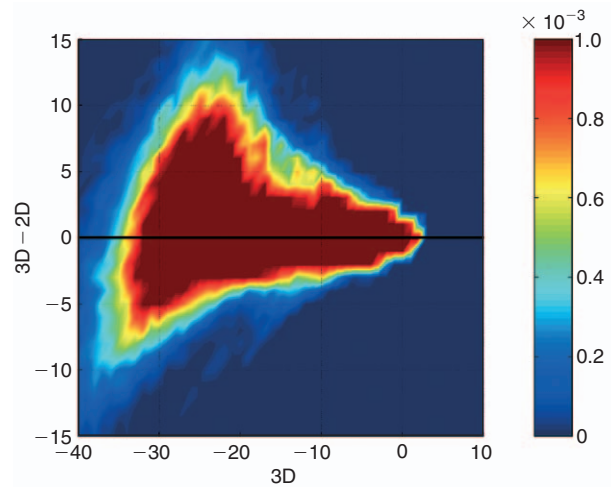

Figure 16. A bivariate histogram of the OWPF decibel difference displayed in Fig. 15 (vertical axis) as a function of the VPE OWPF in decibels (horizontal axis). Results are for the Ni'ihau Island scenario shown in Fig. 13. The polarization is VPOL.

Close agreement between the VPE and P3DTEMPER results is quantitatively demonstrated by the OWPF difference plot at $x = 22$ km shown in Fig. 15 and the OWPF difference histogram in Fig. 16. The histogram indicates that VPE and P3DTEMPER agree to within ± 5 dB at power levels exceeding -15 dB. Larger differences (10 to

To facilitate larger terrain swaths, and thus more general conclusions, a more efficient preconditioned biconjugate gradient (PBCG) iterative scheme must be found to solve the sparse system (Eq. 7) in Domain I of the VPE model. It is well known that the number of iterations needed to achieve convergence in the PBCG procedure scales with the number of field unknowns.[18] Larger terrain swaths result in larger propagation domains and, consequently, a larger number of field unknowns. In addition, the PBCG convergence rate depends on the choice of the preconditioning matrix used in the iterative solution.[19] In the current VPE model, a Jacobi preconditioning matrix is used for simplicity. This preconditioner consists of the diagonal part of the original sparse matrix $\mathbf{A}$; naturally, the Jacobi preconditioner results in fast convergence when $\mathbf{A}$ is diagonally dominated. The off-diagonal elements of $\mathbf{A}$ result from the finite-difference discretization of the boundary condition (Eq. 3), and these elements can become dominant for intricate terrain swaths with steep slopes. In this situation, the Jacobi preconditioner becomes extremely inefficient, and a more effective preconditioner must be developed. The search for the proper preconditioner, as well as the examination of other iterative schemes, will be a main focus of future work.

SUMMARY

This article examined the out-of-plane diffraction and scattering effects of lateral terrain variations on low grazing angle radar propagation over terrain. The 2D propagation model TEMPER does not account for these effects.

Two types of terrain configurations were considered: a simple urban terrain and a digital terrain map. In the urban terrain example, the out-of-plane scattering and diffraction by vertical sides and edges were responsible for a 10- to 20-dB field enhancement over 2D model predictions. These out-of-plane propagation effects were much less pronounced in the digital terrain example. In this case, the agreement between the VPE model and the P3DTEMPER model was within 5 dB at high power levels (OWPF > −15 dB), while the agreement was less favorable for lower levels. These results are not surprising since the out-of-plane scattering and diffraction mechanisms in the urban terrain example are vertical surfaces, which give rise to strong specular scattering and strong, sharp-edge diffraction. On the other hand, in the digital terrain example, the out-of-plane diffraction effects are attributed to surface diffraction, which is a weaker diffraction mechanism. This conclusion must not be generalized without analyzing a wider variety of larger, more intricate digital terrain maps. To facilitate this future work, we plan to enhance the efficiency of our VPE procedure by developing more adequate preconditioners for the PBCG iterative algorithm. This will allow larger terrain swaths to be treated, enabling us to further examine and generalize the observations made in this article.

REFERENCES

[1]Awadallah, R. S., and Brown, G. S., "Low-Grazing Angle Scattering from Rough Surfaces in a Duct Formed by a Linear-Square Refractive Index Profile," *IEEE Trans. Antennas Propag.* **48**, 1461–1474 (2000).

[2]Awadallah, R. S., Lamar, M. T., and Kuttler, J. R., "An Accelerated Boundary Integral Equation Scheme for Propagation over the Ocean Surface," *Radio Sci.* **37**(5), 8-1–8-16 (2002).

[3]Sadiku, M. N. O., *Numerical Techniques in Electromagnetics*, 2nd Ed., CRC Press, New York (2001).

[4]Levy, M., *Parabolic Equation Methods for Electromagnetic Wave Propagation*, IEE, London, UK (2000).

[5]Fock, V. A., *Electromagnetic Diffraction and Propagation Problems*, Pergamon Press, New York (1965).

[6]Hardin, R. H., and Tappert, F. D., "Application of the Split-Step Fourier Method to the Numerical Solution of Nonlinear and Variable Coefficient Wave Equations," *SIAM Rev.* **15**, 423 (1973).

[7]Kuttler, J. R., and Dockery, G. D., "Theoretical Description of the Parabolic Approximation/Fourier Split-Step Method of Representing Electromagnetic Propagation in the Troposphere," *Radio Sci.* **26**, 381–393 (1991).

[8]Donohue, D. J., and Kuttler, J. R., "Propagation Modeling over Terrain Using the Parabolic Wave Equation," *IEEE Trans. Antennas Propag.* **48**, 260–277 (Feb 2000).

[9]Newkirk, M. H., Gehman, J. Z., and Dockery, G. D., "Advances in Calculating Electromagnetic Field Propagation Near the Earth's Surface," *Johns Hopkins APL Tech. Dig.* **22**, 462–472 (2001).

[10]Berenger, J., "A Perfectly Matched Layer for the Absorption of Electromagnetic Waves," *J. Comp. Phys.* **114**(2), 185–200 (Oct 1994).

[11]Rappaport, C. M., "Perfectly Matched Absorbing Boundary Conditions Based on Anisotropic Lossy Mapping of Space," *IEEE Microwave Guided Wave Lett.* **5**(3), 90–92 (Mar 1995).

[12]Smith, G. D., *Numerical Solution of Partial Differential Equations: Finite Difference Methods*, 3rd Ed., Clarendon Press, Oxford (1985).

[13]Zaporozhets, A. A., "Application of the Vector Parabolic Equation Method to Urban Radiowave Propagation Problems," *IEEE Proc. Microwave Antennas Propag.* **146**(4), 253–256 (Aug 1999).

[14]Harrington, R. F., *Time-Harmonic Electromagnetic Fields*, IEEE Press, New York (2001).

[15]Levy, M. F., and Zaporozhets, A. A., "Target Scattering Calculations with the Parabolic Equation Method," *J. Acoust. Soc. Am.* **103**(2), 735 (Feb 1998).

[16]Press, W. H., Teukolsky, S. A., Vetterling, W. T., and Flannery, B. P., *Numerical Recipes in Fortran 77*, 2nd Ed., Cambridge University Press (1992).

[17]Dockery, G. D., "Modeling Electromagnetic Wave Propagation in the Troposphere Using the Parabolic Equation," *IEEE Trans. Antennas Propag.* **36**, 1464–1470 (Oct 1988).

[18]Pocock, M. D., and Walker, S. P., "The Complex Bi-Conjugate Gradient Solver Applied to Large Electromagnetic Scattering Problems, Computational Costs and Cost Scalings," *IEEE Trans. Antennas Propag.* **45**(1), 140–146 (1997).

[19]Saad, Y., *Iterative Methods for Sparse Linear Systems*, Society for Industrial and Applied Mathematics (SIAM), Philadelphia (2003).

THE AUTHORS

RA'ID S. AWADALLAH received B.S.E.E. and M.S.E.E. degrees in 1988 and 1991, respectively, from the Jordan University of Science and Technology, Irbid, Jordan, and a Ph.D. degree in electrical engineering from Virginia Tech, Blacksburg, Virginia, in 1998. From 1991 to 1993, he was a lecturer in the Department of Electronics in the Jerusalem University College of Sciences, Abu-Dis/Jerusalem. In 1998, Dr. Awadallah joined APL and is currently a member of the Senior Professional Staff in the Research and Technology Development Center. His research interests include tropospheric propagation, electromagnetic scattering from randomly rough surfaces, radar cross section of complex targets, and applied electromagnetism. He is a member of the IEEE and Commission F (Wave Propagation and Remote Sensing) of the Union of Radio Science (URSI). His e-mail address is raid.awadallah@jhuapl.edu.

JONATHAN Z. GEHMAN graduated magna cum laude from Cornell University in 1999 with a B.S. in applied and engineering physics and received an M.S. in applied physics (with honors) from The Johns Hopkins University in 2003. Since coming to APL in 1999, he has been involved in physics-based modeling of low-angle radar propagation and backscatter. He is currently co-developer of the latest version of the TEMPER propagation model. His e-mail address is jonathan.gehman@jhuapl.edu.

JAMES R. KUTTLER received a B.A. degree in mathematics from Rice University, Houston, Texas, in 1962, and M.A. and Ph.D. degrees in applied mathematics from the University of Maryland, College Park, in 1964 and 1967, respectively. Since 1967, he has been a mathematician at APL. He is currently a member of the Principal Professional Staff in the Theater Systems Development Group of the Air Defense Systems Department. Dr. Kuttler's areas of expertise are partial differential equations, numerical analysis, finite differences, eigenvalue problems, Fourier analysis, signal processing, chemical phase transitions, synthetic aperture radar, electromagnetics, propagation, scattering and cross-sectional calculations, fractals, and fast convolution algorithms. His e-mail address is james.kuttler@jhuapl.edu.

MICHAEL H. NEWKIRK is a member of the Senior Professional Staff at APL. He received B.S., M.S., and Ph.D. degrees, all from Virginia Tech, in 1988, 1990, and 1994, respectively. Dr. Newkirk held a 1995–1996 postdoctoral fellowship with the U.S. Army Research Laboratory in Adelphi, Maryland, where he performed basic research and design, fabrication, and data analysis for millimeter-wave radiometric systems. Dr. Newkirk joined APL in 1996 and has since been involved in propagation modeling and field test planning and execution. He is a member of the IEEE and the Union of Radio Science (URSI). His e-mail address is michael.newkirk@jhuapl.edu.